

Mind the Gap: Alleviating Local Imbalance for Unsupervised Cross-Modality Medical Image Segmentation

Zixian Su , Kai Yao , Xi Yang , Qiufeng Wang , Member, IEEE, Yuyao Yan, Jie Sun , and Kaizhu Huang , Senior Member, IEEE

Abstract—Unsupervised cross-modality medical image adaptation aims to alleviate the severe domain gap between different imaging modalities without using the target domain label. A key in this campaign relies upon aligning the distributions of source and target domain. One common attempt is to enforce the global alignment between two domains, which, however, ignores the fatal local-imbalance domain gap problem, i.e., some local features with larger domain gap are harder to transfer. Recently, some methods conduct alignment focusing on local regions to improve the efficiency of model learning. While this operation may cause a deficiency of critical information from contexts. To tackle this limitation, we propose a novel strategy to alleviate the domain gap imbalance considering the characteristics of medical images, namely *Global-Local Union Alignment*. Specifically, a feature-disentanglement style-transfer module first synthesizes the target-like source images to reduce the global domain gap. Then, a local feature mask is integrated to reduce the ‘inter-gap’ for local features by prioritizing those discriminative features with larger domain gap. This combination of global and local alignment can precisely localize the crucial regions in segmentation target while preserving the overall semantic consistency. We conduct a series of experiments with two cross-modality adaptation tasks, i.e. cardiac substructure and abdominal multi-organ segmentation. Experimental results indicate

Manuscript received 5 June 2022; revised 26 March 2023; accepted 20 April 2023. Date of publication 3 May 2023; date of current version 3 July 2023. This work was supported in part by National Natural Science Foundation of China under Grants 62276258 and 62206225, in part by the Jiangsu Science and Technology Programme (Natural Science Foundation of Jiangsu Province) under Grant BE2020006-4, in part by the Natural Science Foundation of the Jiangsu Higher Education Institutions of China under Grant 22KJB520039, in part by the Xi'an Jiaotong-Liverpool University's Key Program Special Fund under Grants KSF-E-37 and KSF-T-06, and in part by the Research Development Fund in XJTLU under Grant RDF-19-01-21. (Corresponding authors: Xi Yang; Kaizhu Huang.)

Zixian Su and Kai Yao are with the Department of Electrical Engineering and Electronics, University of Liverpool, Liverpool L69 3BX, U.K., and also with the School of Advanced Technology, Xi'an Jiaotong-Liverpool University, Suzhou 215000, China (e-mail: zixian.su20@student.xjtu.edu.cn; kai.yao19@student.xjtu.edu.cn).

Xi Yang, Qiufeng Wang, Yuyao Yan, and Jie Sun are with the School of Advanced Technology, Xi'an Jiaotong-Liverpool University, Suzhou 215000, China (e-mail: xi.yang01@xjtu.edu.cn; qiufeng.wang@xjtu.edu.cn; joshuayyy@gmail.com; jie.sun@xjtu.edu.cn).

Kaizhu Huang is with the Data Science Research Center, Duke Kunshan University, Kunshan 215316, China (e-mail: kaizhu.huang@dukekunshan.edu.cn).

Digital Object Identifier 10.1109/JBHI.2023.3270434

that our method achieves state-of-the-art performance in both tasks.

Index Terms—Deep learning, semantic segmentation, biomedical imaging.

I. INTRODUCTION

THE success of deep learning models is highly dependent on the assumption that the training and testing data are i.i.d (independently identically distribution). However, in clinical practice, domain shift is widespread among different datasets due to the existence of multiple imaging modalities. Nevertheless, accurate segmentation can only be achieved with a large amount of labeled data in each modality, which is tedious and time-consuming. To tackle this problem, Unsupervised Domain Adaptation (UDA) [1], [2], [3], [4] has been widely investigated to transfer the knowledge learned from a rich-labeled source domain to an unlabeled target domain, so as to train a model to segment the target images without labels.

Although the existing UDA methods have shown impressive results in cross-modality medical image analysis [5], [6], [7], most of them are under the assumption that all features share consistent domain gap. Though the key component of domain adaptation for semantic segmentation is quite straightforward - matching the overall distributions of two different domains, merely focusing on the global distribution gap while ignoring the ‘inter-gap’ of local features appears inappropriate.

For an illustrative example shown in Fig. 1(a), in cardiac segmentation of Magnetic Resonance Imaging (MRI) and Computed Tomography (CT) scans [8], the transfer of knowledge is much easier for Ascending Aorta (AA) as its appearance is quite similar in both domains - they are both brighter than their surroundings, and the shape of this structure is close to each other in two domains. In contrast, the adaptation for the structure MYOcardium (MYO) of the left ventricle will be much harder. The segmentation task for this structure itself is challenging due to the fuzzy boundary, not to mention the difference in morphology and contrast between the two domains. In this kind of scenario, if we only perform basic global alignment without considering the local gap imbalance, a possible consequence would be the over-alignment for the transferable features and insufficient adaptation for the discriminative features, as shown in Fig. 2.

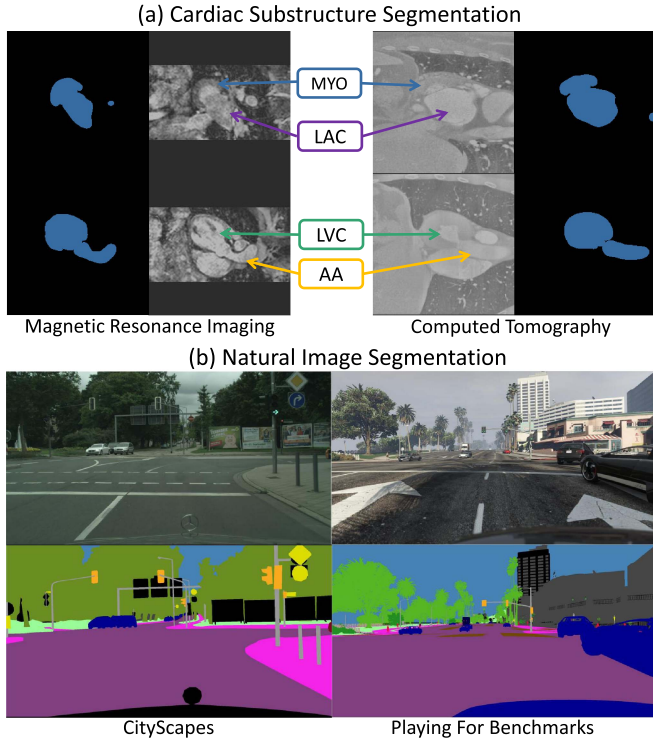


Fig. 1. Severe domain gap can be seen in cross-modality cardiac dataset, as compared with natural images. Except for the style difference in two modalities, substructures show diverse morphology. This phenomenon is more obvious for MYO and LVC, which indicates larger domain gap in these local regions.

Here, the transferable features indicate those with a relatively small domain gap (cross samples in Fig. 2), while the discriminative features represent the ones with a larger domain gap (circle samples in Fig. 2). A bigger cost would be the misalignment of local features in order to achieve strict global alignment, in which the local features ‘inter-gaps’ may even be enlarged.

In [9], Chen et al. shared the similar view that strictly aligning the entire feature distributions between domains is prone to result in negative transfer, since the transferability of different levels varies greatly. In addition, in [10], Saito et al. identified an analogous phenomenon for object (instance-level) and scene layouts (image-level) in the task of object detection. Therefore, Chen et al. proposed to handle a contradiction between transferability and discriminability globally and locally, while [10] chose to leverage strong-local and weak-global alignment strategy instead.

In a similar spirit, we rethink the alignment strategy for domain gap problem in medical image data. In this study, our main goal is to improve the transferability of the segmentation object. Considering that the characteristics of medical images are quite different from those natural images [11], [12] - the segmentation target is relatively small and centralized, while the background is comparably complex and different (see Fig. 1(a) and (b)), the domain shift problem itself is more severe and challenging, as it implies that not only the segmentation target but also the irrelevant background has a large domain shift. Due to the one-of-a-kind existence of irrelevant and complex background,

the performance of common attempts on natural datasets would be greatly reduced. In other words, the key issue is effective alignment in the segmentation target with local domain gap imbalance. Thus, we argue that global alignment as well as the local alignment are both essential for domain adaptation in medical images. Merely global alignment may hurt the overall performance, potentially impairing the discriminability in target domain. While local alignment itself is insufficient to capture discriminative features in the segmentation target, it is likely to act on background area incorrectly under severe domain shift. Therefore, we first introduce a style-transfer module to pre-process the data beforehand to conquer the severe domain shift in the whole picture, as illustrated in Fig. 2. This step proves vital, since it can make alignment at the domain level to globally alleviate the domain shift both in background and target, helping the downstream module prioritize the discriminative features with larger domain gap in the segmentation target instead of those in the whole picture. After that, the local feature masks are adopted in segmentation subnet produced by the uncertainty of the domain discriminator, which can be seen as the attention-like module that identifies the local domain gap in feature space unsupervisedly. This module could capture the discriminative features and emphasize these local alignment, ensuring the local-level semantic consistency for final prediction.

To sum up, the framework is capable of paying more attention to local regions with larger variance in segmentation target instead of coarse global alignment. Our main contributions are highlighted as follows:

- 1) We propose a novel strategy, Global-Local Union Alignment, which combines global alignment and local alignment while considering the characteristics of medical images, thereby promoting the overall transferability in cross-modality tasks with severe domain gap and local gap imbalance.

- 2) The results in two bidirectional cross-modality segmentation tasks between MRI and CT: cardiac substructure segmentation [8] and abdominal multi-organ segmentation [13], [14] demonstrate that our method achieves superior performance to state-of-the-art UDA methods generally.

II. RELATED WORK

1) Domain Adaptation in Medical Image Analysis: There has been a rapid development of deep learning models for medical image analysis [15], [16], [17]. Nonetheless, the effectiveness of deep learning model in the clinical application has been greatly hindered due to the requirement of a large amount of labeled data and the population of multi-modality datasets. To solve these problems, several Unsupervised Domain Adaptation (UDA) methods have been proposed and achieved great performance for medical datasets [5], [6], [18]. By leveraging the shared features between the source and target domains, UDA effectively transfers knowledge from the former to the latter, thereby alleviating the need for extensive labeling efforts. This approach not only enhances the model’s performance but also reduces the overall cost and time required for data acquisition and annotation, making it an attractive option for medical professionals seeking to streamline their workflows and improve patient outcomes.

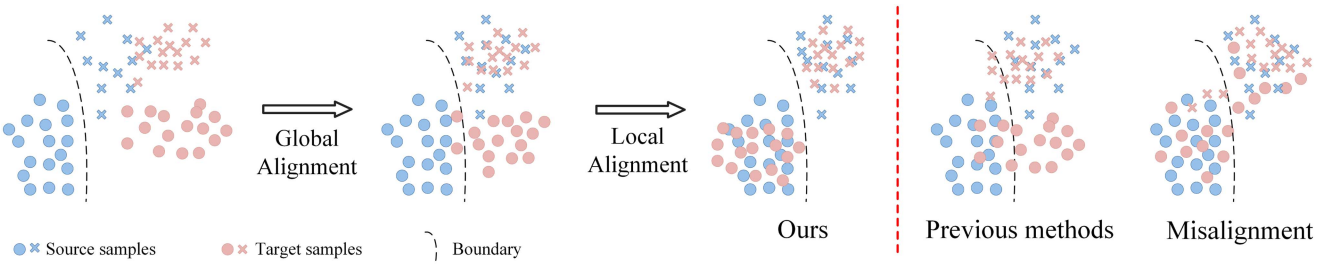


Fig. 2. Illustration of our proposed method vs. global alignment.

For example, Wollmann et al. [19] proposed a CycleGAN-based domain adaptation method for breast cancer classification. Similarly, this mode was also leveraged by Manakov et al. [20] to tackle the retinal Optical Coherence Tomography (OCT) image denoising problem. Mahmood et al. [21] proposed a reverse unsupervised domain adaptation method to generate a synthetic-like representation of real endoscopy images for the notoriously difficult task of depth-estimation from endoscopy. Recently, Chen et al. [22] presented a novel UDA network for semantic segmentation which synergistically combines feature alignment and image alignment into one unified framework to improve the adaptation performance. Some of the latest work [23], [24] even exploited networks pretrained on large-scale datasets which could leverage pretext knowledge to further boost performance on medical UDA tasks.

2) Global Alignment Vs. Local Alignment: The existing UDA methods can mainly be divided in three categories, adversarial training [25], [26], distance minimization [27], [28] and self-training [29], [30]. These classical methods align the global source and target domain distribution without considering the class/local-level distribution shift imbalance, which, however, leads some discriminable class-wise/local information to be confused. Recently, researchers are increasingly investigating local-level alignment [31], [32], which performs local alignment of the source and target domains in the feature space leveraging the uncertainty of the model. These alignment methods have gained considerable performance improvement compared with the conventional ones in common datasets due to capturing the fine-grained domain information. Besides, the combination of global and local alignment are undoubtedly arising research attention. Except for [9], [10] stated above which consider global and local alignment at multi-level feature space with various size of respective fields, [33] proposed contextual-relationships consistent domain adaptation via multi-scale entropy max-minimizing; and [34] adopted robust local preserving and global aligning network under the setting of noisy labels. Our framework is similar to [9], [10] in that the local alignment module is introduced to reflect the discriminability and calibrate the transferability of feature representations. However, the proposed method is much different from them both in global alignment strategy and the interaction method between global and local alignment. [9], [10] made local alignment with a small receptive field in feature space and global features (image-size) on deeper layers of the model, with both alignments unified in one stage. The global alignment in our work is operated on the whole distribution at domain level,

which can be taken as a preprocessing step ahead of the local alignment.

III. MAIN METHOD

A. Method Overview

In this work, we focus on the UDA problem for medical image semantic segmentation, where the labeled source dataset $\{x_s, y_s\}$ and unlabeled target set $\{x_t\}$ are available.

The overall framework is shown in Fig. 3, which is composed of a synthesis subnet and a segmentation subnet, each designed to address a specific challenge of cross-domain medical image segmentation. The first stage of the framework involves the synthesis subnet, which preprocesses the data to achieve global domain-level alignment, mitigating the domain shift in both the background and target. Specifically, the network first disentangles the features of two domains into a shared content space and individual style representations. By swapping the individual style representation to exchange the style of the original image, the style-transferred images are generated with the anatomical structure maintained. This global alignment allows the downstream segmentation subnet to focus on local discriminative features with a larger domain gap in the segmentation target. In the second stage, the segmentation subnet employs a local alignment module that leverages the feature masks generated by the uncertainty of the domain discriminator. The attention mechanism allows the network to identify and emphasize the discriminative local features, promoting local-level transferability to further improve the adaptation. To be precise, the style-transferred source domain image $x_{s \rightarrow t}$ and the original target domain image x_t are fed into the segmentation subnet. With a local feature mask computed by a pixel-wise domain discriminator, the target domain feature is reweighted and calibrated. The convolutional segmentor can attain more accurate prediction by concentrating on the discriminable features with larger domain shift, balancing the ‘inter-gap’ between local features. The following sections provide a detailed description of the entire process.

1) Global Alignment: Feature-Disentanglement Synthesis Subnet: Similar to the ideas of predominant image transformation methods [35], [36], we assume that the latent space of images can be decomposed into a content space and a style space. While in our framework, rather than taking a single domain as diverse styles, we employ a unified domain style instead. Following this assumption, the image $x_i \in \mathcal{X}_i (i = s, t)$ can be represented as $x_i = (c_i, d_i)$, where c_i is the content

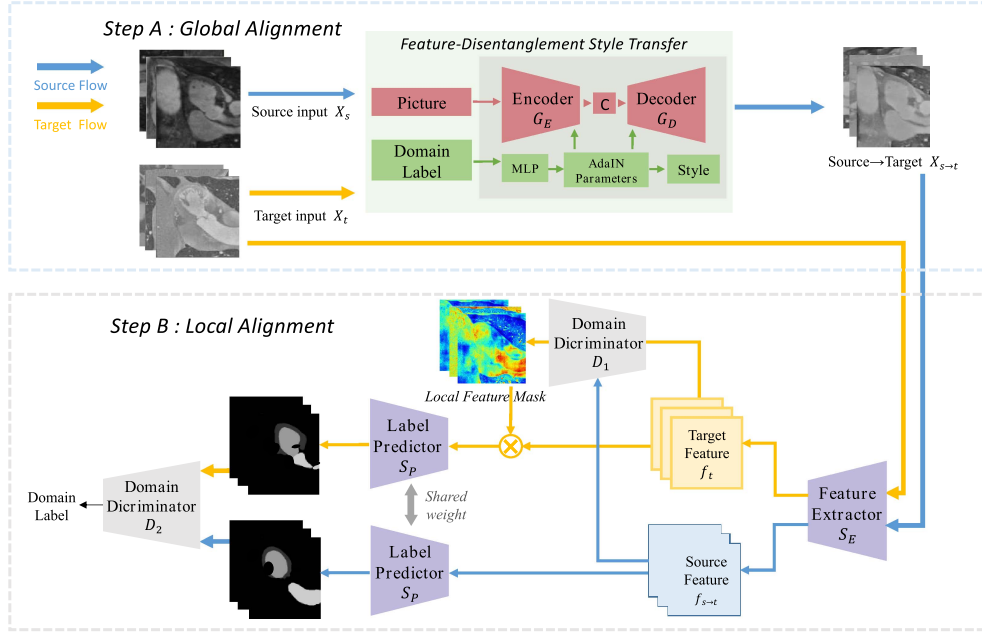


Fig. 3. Overview of the whole framework. The feature-disentanglement style-transfer subnet first synthesizes the source-content target-style images. Combined with real target images, they are used to train the segmentation subnet, where a local feature mask is introduced to calibrate the discriminative areas. The module C in step A is the ‘content’(domain-invariant features) of an image.

representation of image x_i and d_i is the style representation - domain label. Different from previous efforts that use an extra encoder to extract the domain-specific features to represent style, our work employs a Multi-Layer Perceptron (MLP) to learn the style representation for each domain, which is represented by the domain label d_i . Inspired by some recent work that engages affine transformation parameters in normalization layers to represent styles, we equip both the decomposition and reconstruction processes with Adaptive Instance Normalization (AdaIN) [37] layers to introduce the style representations.

As shown in Fig. 3, we exploit a 2D auto-encoder architecture as the synthesis subnet \mathcal{G} , which consists of a shared encoder \mathcal{G}_E and decoder \mathcal{G}_D . First, the content representation c_x of the image x is obtained using encoder \mathcal{G}_E conditioned on the domain label d_i , i.e., $c_i = \mathcal{G}_E(x_i, d_i)$. Then, we compose the reconstructed image x_{ii} based on the content c_x and domain label d_i , i.e., $x_{ii} = \mathcal{G}_D(\mathcal{G}_E((x_i, d_i)), d_i)$. Similarly, the style-transferred image (from domain i to domain j) can be integrated as $x_{ij} = \mathcal{G}_D(\mathcal{G}_E((x_i, d_i)), d_j)$, $i \neq j$. In addition, a Markovian discriminator [38] D is introduced as the image discriminator for both domains, which learns to determine whether an image x_i is a real image of its domain \mathcal{X}_i or a fake one generated by \mathcal{G} , i.e., $D_i(x_i) = D(x_i | d_i)$. More details of the structure and hyperparameters of the synthesis subnet can be found in the appendix.

2) Local Alignment: Segmentation Subnet With Dual Discriminators: As shown in Fig. 3, local alignment stage is mainly composed of a segmentation network S and two discriminator networks D_1, D_2 . For better description, the segmentation network can be further decomposed into two compositions, a feature extractor S_E and a label predictor S_P . We adopt Deeplab-ResNet50 [39] as the segmentation backbone. Discriminators are two convolutional classifiers working in feature space and image space respectively. The target-like source-content images

$x_{s\rightarrow t}$ will be first extracted by S_E to form the feature representation $f_{s\rightarrow t}$, i.e., $f_{s\rightarrow t} = S_E(x_{s\rightarrow t})$. Then the feature map $f_{s\rightarrow t}$ will be taken into the label predictor S_P for semantic segmentation to get the final result $p_{s\rightarrow t}$. Meanwhile, the feature map $f_{s\rightarrow t}$ and final prediction $p_{s\rightarrow t}$ are input into the discriminators as the source samples of adversarial training, respectively.

For the real target flow, the feature map f_t extracted by S_E is first fed into D_1 . D_1 will evaluate the feature distribution of target data f_t and produce a local feature mask m , where $m = |D_1(f_t)|$. The feature mask then reweights the original feature map f_t to form a new feature map $\hat{f}_t = f_t + f_t \otimes \text{expand}(\tanh(m))$ and feeds it into S_P to yield the final prediction. Here, expand operation replicates the local feature map with channel 1 to a channel dimension that is the same as the input feature for the subsequent element-wise multiplication and \tanh is introduced as a normalization layer to prevent the gradient exploration in the early training stage. For the second discriminator D_2 , it evaluates the final predictions calibrated through the feature mask m , and further narrows the pixel-level domain gap between source prediction p_s and target prediction p_t through adversarial loss.

B. Objective Function

The proposed model is featured in two stages. In stage one, the training loss consists of reconstruction loss, cycle consistency loss, and adversarial loss. First of all, the reconstruction loss \mathcal{L}_{rec} is a promise for the synthesis net \mathcal{G} to rebuild the image x_i and content c_i during cross-domain translation:

$$\begin{aligned}\mathcal{L}_{rec_im}(\mathcal{G}_E, \mathcal{G}_D) &= \mathbb{E}_{x_i \sim p(X_i)} [\|\mathcal{G}_D(\mathcal{G}_E(x_i, d_i), d_i) - x_i\|_1], \\ \mathcal{L}_{rec_c}(\mathcal{G}_E, \mathcal{G}_D) &= \mathbb{E}_{c_i} [\|\mathcal{G}_E(\mathcal{G}_D(c_i, d_j), d_j) - c_i\|_1].\end{aligned}$$

Meanwhile, a cycle-consistency loss is adopted to guarantee that the mapping between the original image and the generated image is a unique cross-domain. Namely, for a given image x_i , it should return to itself when translated $\mathcal{X}_i \rightarrow \mathcal{X}_j \rightarrow \mathcal{X}_i$. The cycle-consistency loss is described as:

$$\begin{aligned}\mathcal{L}_{cyc}(\mathcal{G}_E, \mathcal{G}_D) = \\ \mathbb{E}_{x_i \sim p(X_i)} [\|\mathcal{G}_D(\mathcal{G}_E(\mathcal{G}_D((\mathcal{G}_E(x_i, d_i), d_i), d_j), d_i) - x_i\|_1].\end{aligned}$$

Moreover, we would like to make sure that the data x_{ij} generated by \mathcal{G} is as close to the real data distribution as possible, an adversarial loss is included in GAN training with the domain discriminator D :

$$\begin{aligned}\mathcal{L}_{adv}(\mathcal{G}, D) = \mathbb{E}_{x_j \sim p(X_j)} [\log D((x_j | d_j)] \\ + \mathbb{E}_{x_i \sim p(X_i)} [1 - \log D(\mathcal{G}_D(\mathcal{G}_E(x_i, d_i), d_j) | d_j)].\end{aligned}$$

Finally, we jointly train the encoder, decoder, and domain discriminator, which is shown as:

$$\begin{aligned}\min_{\mathcal{G}_E, \mathcal{G}_D} \max_{\mathcal{D}} \lambda_{rec_im} \mathcal{L}_{rec_im} + \lambda_{rec_c} \mathcal{L}_{rec_c} \\ + \lambda_{cyc} \mathcal{L}_{cyc} + \lambda_{adv} \mathcal{L}_{adv}.\end{aligned}$$

In stage two, the training loss is composed of the segmentation loss and adversarial loss. Segmentation loss \mathcal{L}_{seg} is for segmentor $S(\mathcal{S}_E, \mathcal{S}_P)$ to output more accurate prediction in a supervised way:

$$\begin{aligned}\mathcal{L}_{seg}(\mathcal{S}_E, \mathcal{S}_P) = \mathbb{E}_{x_i, y_i \sim p(X_S, Y_S)} (\ell_{ce}(\mathcal{S}(x_i), y_i) \\ + \ell_{dice}(\mathcal{S}(x_i), y_i)).\end{aligned}$$

ℓ_{ce} and ℓ_{dice} term represent the multi-class cross-entropy loss and the Dice loss.

The adversarial loss can be decomposed into two parts, $\mathcal{L}_{adv}^{D_1}(\mathcal{S}_E, D_1)$ and $\mathcal{L}_{adv}^{D_2}(\mathcal{S}_E, \mathcal{S}_P, D_2)$, indicating the adversarial learning losses of the two discriminators, respectively. The process is summarized as below:

$$\begin{aligned}\mathcal{L}_{adv}^{D_1}(\mathcal{S}_E, D_1) = \mathbb{E}_{x_{s \rightarrow t} \sim p(X_{S \rightarrow T})} [\log D_1(\mathcal{S}_E(x_{s \rightarrow t})) \\ + \mathbb{E}_{x_t \sim p(X_T)} [1 - \log D_1(\mathcal{S}_E(x_t))]. \\ \mathcal{L}_{adv}^{D_2}(\mathcal{S}, D_2) = \mathbb{E}_{x_{s \rightarrow t} \sim p(X_{S \rightarrow T})} [\log D_2(\mathcal{S}(x_{s \rightarrow t})) \\ + \mathbb{E}_{x_t \sim p(X_T)} [1 - \log D_2(\mathcal{S}(x_t))].\end{aligned}$$

The overall training objective function of the segmentation subnet is:

$$\begin{aligned}\min_{\mathcal{S}_E, \mathcal{S}_P} \max_{D_1, D_2} \mathcal{L}_{seg}(\mathcal{S}_E, \mathcal{S}_P) + \lambda_{d_1} \mathcal{L}_{adv}^{D_1}(\mathcal{S}_E, D_1) \\ + \lambda_{d_2} \mathcal{L}_{adv}^{D_2}(\mathcal{S}_E, \mathcal{S}_P, D_2).\end{aligned}$$

λ_{rec_im} , λ_{cyc} , λ_{rec_c} , λ_{adv} , λ_{d_1} , λ_{d_2} are introduced to balance the relative importance of different terms.

IV. EXPERIMENTS

A. Setup

1) **Implementation Details:** Our model is implemented using PyTorch toolbox on a Quadro RTX 8000 (48 GB memory).

In style-transfer stage, ADAM solver [46] is adopted with a batch size of 8. Learning rate is set to 0.0002, and weight decay is 0.0001. In the segmentation stage, we choose SGD algorithm as the optimizer for segmentator \mathcal{S} with momentum of 0.9 and weight decay of 0.0005, while for the dual discriminators we use ADAM optimizer with $\beta_1 = 0.9$ and $\beta_2 = 0.99$. The weight decay method is polynomial decay with a power of 0.9. All the networks are trained from scratch. We tune the batch size and learning rate empirically in each task. For the hyper-parameters, $\lambda_{rec_im} = \lambda_{cyc} = 20$, $\lambda_{rec_c} = \lambda_{adv} = 1$, $\lambda_{d_1} = \lambda_{d_2} = 0.01$. We train the style-transfer model for 50 k iterations. After that, the pre-processed training set is fed into the segmentation network. The validation set is used to find the model with the best performance.

2) **Datasets:** Two challenging adaptation tasks, e.g., Cardiac substructure segmentation and Abdominal multi-organ segmentation, are performed in the experiment. 1) Cardiac substructure segmentation utilizes the Multi-Modality Whole Heart Segmentation (MMWHS) Challenge 2017 dataset [8], which is composed of 20 labeled MRI volumes and 20 labeled CT volumes. The goal is to parse four heart structures: the Ascending Aorta (AA), the Left Atrium Cavity (LAC), the Left Ventricle blood Cavity (LVC) and the MYOcardium (MYO) of the left ventricle. The minority classes are the MYO and AA, compared with the LAC and LVC. 2) Abdominal multi-organ segmentation is implemented with 30 volumes CT data from [14] and 20 volumes of T2-SPIR MRI data from ISBI CHAOS Challenge 2019 [13] with both groundtruth masks provided. We aim to segment the four key organs, including liver, right kidney, left kidney and spleen. Except for the liver, the remaining three classes take up a small proportion of the overall region.

The pre-processing includes normalization, random crop, rotation and other augmentation operations. The size for each slice is 256×256 in the cardiac dataset and 512×512 in the abdominal dataset. For cardiac dataset, we used the pre-processed version from [22]. It is worth noting that two domains of pictures in both tasks are unpaired.

3) **Evaluation Indicators:** Two metrics commonly used in medical image segmentation are adopted: Dice similarity coefficient (Dice) and the Average Surface Distance (ASD). Dice score measures the voxel-level intersection part between the prediction mask and the ground truth mask, while the ASD coefficient represents the average distances between the surfaces of the two in 3D.

B. Experimental Results

We evaluate quantitatively and qualitatively our method against other SOTAs including CycleGAN [3], CyCADA [40], SynSeg-Net [5], SIFA [22], DSFN [41], UESM [44], DSAN [24], CUDA [45], DDA-GAN [42] and UMDA [43]. Among them, the earlier methods CycleGAN and SynSeg-Net conduct adversarial alignment at the pixel level, while the remaining methods exploit both image and feature alignment.

Tables I, II and Figs. 4, 5 respectively show the comparison results in cardiac segmentation and abdominal multi-organ segmentation. Part of the lines are absent due to the lack of public

TABLE I
PERFORMANCE COMPARISON OF DIFFERENT METHODS FOR CROSS-MODALITY CARDIAC SEGMENTATION

Method	Cardiac MRI - CT								Cardiac CT - MRI								ASD(voxel) ↓			
	Dice(%) ↑				ASD(voxel) ↓				Dice(%) ↑				ASD(voxel) ↓				ASD(voxel) ↓			
	AA	LAC	LVC	MYO	Avg	AA	LAC	LVC	MYO	Avg	AA	LAC	LVC	MYO	Avg	AA	LAC	LVC	MYO	Avg
Supervised training	88.49	87.71	90.69	83.33	87.55	3.64	3.19	2.03	2.14	2.75	83.61	84.16	90.74	76.40	83.73	1.98	1.73	1.58	1.64	1.73
No adaptation	30.75	26.25	10.10	1.36	17.12	26.92	18.45	16.75	28.78	22.73	12.79	11.52	10.21	8.61	10.78	11.74	11.21	14.10	11.23	12.07
CycleGAN [3]	72.58	71.88	50.45	31.52	56.61	12.50	14.76	9.08	8.48	11.21	61.90	40.97	60.27	41.59	51.18	5.83	8.43	7.84	5.12	6.81
SynSeg-Net [5]	66.99	62.11	47.20	38.00	53.58	12.85	8.19	7.31	10.22	9.64	58.50	39.09	62.49	31.10	47.80	9.55	10.03	7.81	5.04	8.10
CyCADA [42]	68.18	64.23	48.90	44.89	56.55	9.69	10.36	9.41	11.77	10.34	59.65	42.77	62.21	36.90	50.38	8.40	12.19	6.09	6.26	8.23
SIFA [20]	81.30	79.50	73.80	61.60	74.10	7.90	6.20	5.50	8.50	7.00	65.30	62.30	78.90	47.30	63.40	7.30	7.40	3.80	4.40	5.70
DSFN [43]	84.70	76.90	79.10	62.40	75.80	-	-	-	-	-	-	-	-	-	-	-	-	-	-	-
DDA-GAN [44]	68.30	75.70	78.50	77.80	75.10	6.50	4.80	5.40	5.20	5.50	-	-	-	-	-	-	-	-	-	-
UMDA [45]	89.20	82.70	82.60	66.20	80.20	6.70	3.60	4.50	3.00	4.00	-	-	-	-	-	-	-	-	-	-
UESM [46]	84.15	88.30	84.32	71.42	82.05	3.87	3.49	3.81	3.70	3.71	-	-	-	-	-	-	-	-	-	-
DSAN [26]	79.92	84.76	82.77	66.52	78.50	7.68	6.65	3.77	5.59	5.92	71.29	66.23	76.20	52.07	66.45	4.44	7.30	5.46	4.25	5.36
CUDA [47]	87.20	88.50	83.00	72.80	82.90	7.03	2.80	5.20	6.80	5.50	68.50	66.10	79.10	42.80	65.50	5.10	4.10	3.20	4.10	4.10
Ours (Avg)	87.18	85.47	87.03	70.28	82.49	4.65	3.59	3.50	3.09	3.71	70.01	69.02	85.30	54.05	69.60	5.14	3.16	2.55	3.45	3.58
Standard deviation	0.74	1.52	1.53	1.50	-	0.09	0.23	0.17	0.19	-	0.80	1.19	0.47	0.71	-	0.47	0.50	0.20	0.04	-

TABLE II
PERFORMANCE COMPARISON OF DIFFERENT METHODS FOR CROSS-MODALITY ABDOMINAL SEGMENTATION

Method	Abdominal MRI - CT								Abdominal CT - MRI								ASD(voxel) ↓			
	Dice(%) ↑				ASD(voxel) ↓				Dice(%) ↑				ASD(voxel) ↓				ASD(voxel) ↓			
	Liver	R.kid	L.Kid	Spleen	Avg	Liver	R.kid	L.Kid	Spleen	Avg	Liver	R.kid	L.Kid	Spleen	Avg	Liver	R.kid	L.Kid	Spleen	Avg
Supervised training	95.08	91.06	93.62	89.37	92.28	0.66	1.18	0.73	1.11	0.92	93.21	93.42	93.22	89.59	92.36	0.70	0.48	0.55	1.12	0.71
No adaptation	78.65	54.52	47.84	55.48	59.12	3.86	8.72	3.19	4.88	5.16	58.30	61.08	59.85	73.95	63.30	3.93	1.82	2.58	2.42	2.69
SynSeg-Net [5]	82.15	79.36	68.06	80.44	77.50	2.67	1.98	2.09	2.65	2.34	84.30	88.61	71.92	74.39	79.81	2.94	1.86	2.33	2.51	2.41
CyCADA [42]	81.08	75.95	73.69	76.13	76.71	2.24	1.96	1.94	1.74	1.97	85.72	88.56	75.51	78.46	82.06	2.74	2.16	1.91	2.29	2.28
SIFA [20]	88.00	83.30	80.90	82.60	83.70	1.20	1.00	1.50	1.60	1.30	90.00	89.10	80.20	82.30	85.40	1.50	0.60	1.50	2.40	1.50
CycleGAN [3]	82.47	76.94	78.28	78.89	79.15	1.68	1.35	1.90	1.94	1.71	87.33	88.39	74.28	80.91	82.72	2.05	2.59	1.84	2.87	2.34
DSAN [26]	-	-	-	-	-	-	-	-	-	-	89.30	90.16	90.09	89.84	89.84	-	-	-	-	-
Ours (Avg)	93.76	85.44	87.62	93.85	90.17	1.47	3.21	1.81	1.65	2.04	90.01	92.19	90.17	93.47	91.46	1.20	0.38	0.35	0.33	0.57
Standard deviation	0.88	0.20	0.90	0.63	-	0.23	0.36	0.22	0.14	-	0.49	0.88	0.75	0.63	-	0.07	0.05	0.10	0.04	-

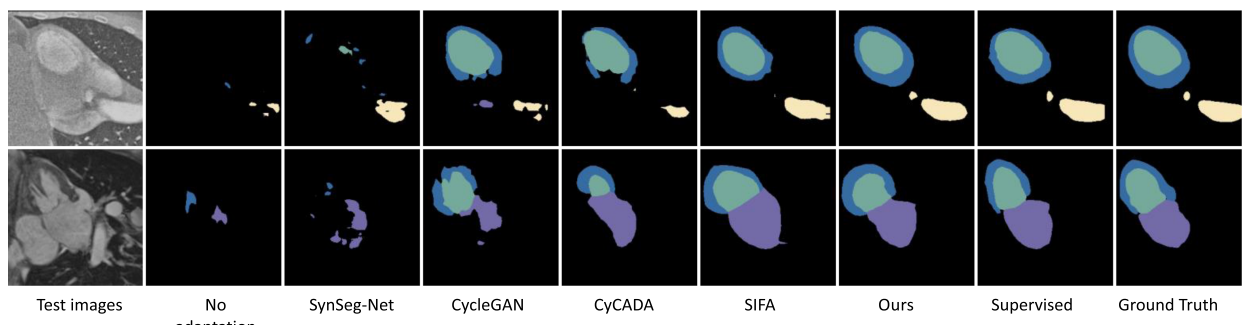


Fig. 4. Qualitative comparison result of cardiac segmentation. The first row are CT images and the following row are MR images. The cardiac substructure, AA, LAC, LVC, MYO are marked in yellow, purple, green and blue, respectively.

codes. We conduct CycleGAN, SynSeg-Net and CyCADA on our datasets to obtain the final numbers. Performance of the remaining methods come from their papers. It is also noted that all the reported results use the unpretrained backbones for fair comparison. We also provide the results without adaptation and supervised training for comparison, where only a segmentation backbone is adopted. These two results can be approximately regarded as the lower and upper bounds for UDA.

From these results, it can be seen that 1) There is a drastic performance drop between no adaptation and supervised training, indicating that a large domain gap exists between two domains in both tasks. 2) Our proposed method outperforms current state-of-the-art methods generally. Compared with CyCADA [40], which takes a similar two-stage setting but conducts global alignment only, our method improves the Dice score from 56.55% to 82.49% in Cardiac MRI → CT segmentation. Although our method (82.49%) is slightly inferior to CUDA (82.90%) in task

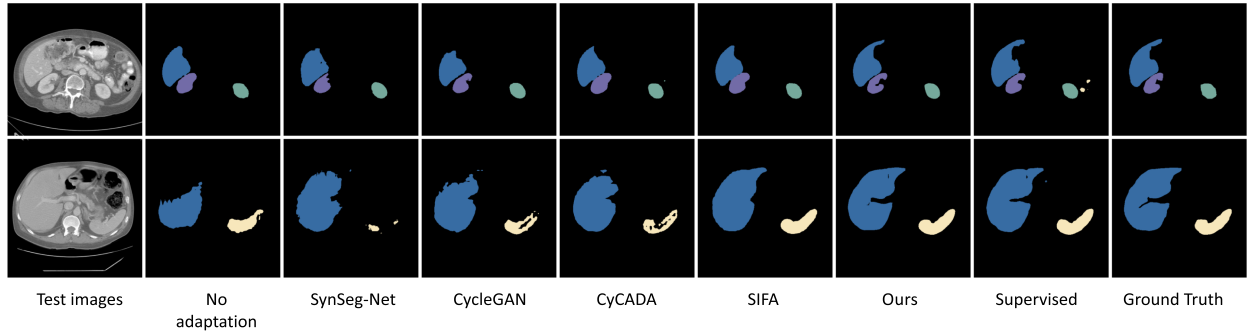


Fig. 5. Qualitative comparison results of abdominal segmentation. The first row are MR images, and the following one are CT images. The organs, Liver, Right kidney, Left kidney and Spleen, are marked in blue, purple, green and yellow, respectively.

TABLE III
ABLATION STUDY OF KEY COMPONENTS IN CARDIAC MRI - CT

StarGAN-v2	-	-	-	-	-	✓	-	-
CycleGAN	-	-	-	-	-	-	✓	-
Style-Transfer	-	✓	✓	✓	-	-	-	✓
D_1	-	-	✓	-	✓	✓	✓	✓
D_2	-	-	-	✓	✓	✓	✓	✓
Dice(%)	17.12	58.35	78.51	60.52	68.76	70.70	81.17	82.49

Cardiac MRI-CT, it exceeds CUDA by a large margin in the inversed direction (Ours 69.60% vs. CUDA 65.50%). The main reason may be the superiority of their segmentation backbone, which accounts for the major contributions of their work. Moreover, the results on the abdominal dataset further corroborate the effectiveness of our method. Although our method generally outperforms other approaches, it is worth noting that the ASD result for the directional MRI-CT alignment on the abdominal multi-organ dataset is comparatively poor. This discrepancy may be attributed to the use of different annotation criteria for MRI and CT images. For instance, the annotation of the kidney is hollow in MRI but filled in CT as shown in the last columns in Figs. 11, 12. 3) Our method appears to perform better in classes with larger domain gaps. Regions with lower transferability are more likely to appear in classes with larger domain gap, which was empirically derived from our observations of the local feature masks. As in MYO of Cardiac MRI \rightarrow CT and LVC of CT \rightarrow MR, our method exhibits more improvements than other classes in the same task.

C. Analysis

1) Effectiveness of Key Components: To verify the influence of each module in our network, we conduct ablation tests on cardiac MRI \rightarrow CT segmentation task, as reported in Table III. With the style-transfer pre-processing, the Dice score raises 41.23% compared with no adaptation. The dual discriminators of local alignment module bring an improvement from 17.12% to 68.76% in Dice. Moreover, D_1 improves 20.16% and D_2 improves 2.17% when individually adopted with the style-transfer module. If two modules are combined, the final outcome can achieve an astonishing result of 82.49%.

Besides demonstrating the effectiveness of each module and their mixtures by numerical values, we provide the visualization

of the local feature mask, serving as the indicator for local feature domain gap in Fig. 6. We can infer that 1) the style-transfer step can significantly reduce the domain gap globally, especially in the background. By comparing the feature mask of the second and third columns, in the absence of global alignment, the discriminator tends to output high uncertainty in the background and considers it as part of discriminative region, thus the vital segmentation target obtains relative low scores. In this situation, the local alignment module is meaningless as aligning the background area will not contribute to final prediction. However, when the style-transfer step is adopted, the third column indicates the downstream modules can better capture discriminative features in segmentation target. 2) the discriminator D_1 could provide accurate feedback on the region with larger domain gap, and by adaptively re-weighting the feature map, prediction performance is improved accordingly. When comparing the feature mask with the SOTA results, we observe a peak in the feature mask regions that corresponds to the areas where SOTAs do not predict accurately. This shows our module is able to locate the real discriminative regions precisely. Then, if we add our prediction in comparison, our method performs apparently better in these areas, indicating the effectiveness of our local alignment module.

2) Choice of Style Transfer: We provide visualization examples in Fig. 7 to compare our style-transfer methods with other SOTA style-transfer methods [3], [36], [47], [48]. The aim of style-transfer pre-processing is to reduce the domain gap from a stylistic perspective globally, weakening the influence of different backgrounds on the subsequent local alignment. The downstream discriminator would better focus on the segmentation target. Therefore, we design the network according to the following criteria: 1) the synthesized image should be indistinguishable in style from the target domain, and 2) the semantic content of domain should be well preserved. Although it is hard to define the explicit content/style in different domains due to the deformation of structure appearance in our datasets, we assume source domain and target domain share the same content but different styles. The domain-invariant feature is taken as content that reveals the target's spatial structure, and the rendering of the structure is regarded as the style.

Visualization of different style transfer methods shows that 1) Compared with CycleGAN [3], our style-transfer method

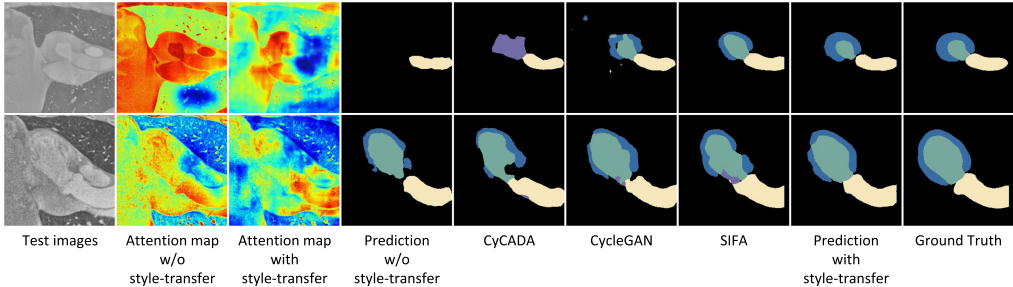


Fig. 6. Visualization of the relation between local feature masks and transferability in different methods.

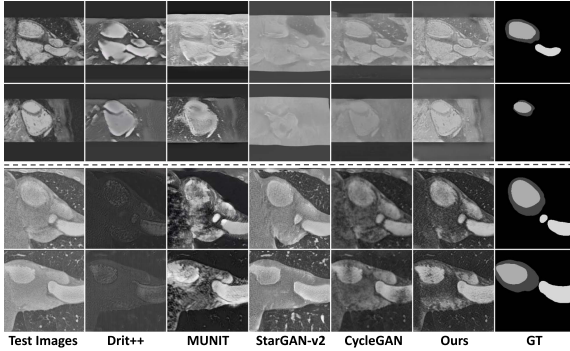


Fig. 7. Comparison of style-transfer. The first two rows are MRI → CT examples. The last two rows are CT → MR examples.

utilizing a feature-disentangling strategy can better preserve the semantic information, revealing the effectiveness of the disentanglement; 2) Methods working well on natural image data fail to obtain satisfactory results. We believe that the methods with too strong style-transfer ability are not applicable to medical image datasets, partially due to the difficulty distinguishing the style and content in medical images. For MUNIT [36], Drit++ [47] and StarGAN-v2 [48], structure deformation is quite likely as they use a sample-level training strategy. The large intra-domain variance adds the risk of negative transfer in this setting. Instead, utilizing an average style for an entire domain seems relatively safe in our scenario.

Based on the qualitative results obtained, we further examine quantitatively two style transfers, e.g. StarGAN-v2 [48] and CycleGAN [3] on how they affect subsequent segmentation. The results are reported in Table III. As observed, our method still achieves the best performance.

3) Limitation: Strictly from the perspective of feature disentangling, the shape variance of the same structure in cross-modality datasets should be taken as part of domain-specific features. Our strategy is to utilize the average style of a domain to attain relatively stable results. This method is valid in our experiment, as the same substructure even shows diverse shapes in the same domain in our tasks. We suspect the network could notice this variation when picking the average style. However, supposing that a single class has a fixed shape in one domain and shows different morphology in another, this method is no longer appropriate. This is because it is likely to regard its shape change

as style difference between domains. It consequently produces deformed images and impacts the subsequent segmentation negatively.

V. CONCLUSION

In this paper, we propose a novel strategy to better solve the domain adaptation problems in medical image datasets. By jointly aligning the domains globally and locally, the model can not only reduce the global domain shift, but also alleviate the inter-gap problem for local features. The local alignment could calibrate the local transferability, especially in crucial areas in segmentation target, thus promoting the overall performance. We validate the proposed framework with two challenging tasks, cardiac and abdominal segmentation, and the experimental results achieve comparable even superior performance to the state-of-the-art domain adaptation methods.

APPENDIX

A. Additional Results

We present more qualitative result for our experiments with cardiac dataset and abdominal dataset. In Figs. 9 and 10, we show additional result in cardiac substructure segmentation. Similarly, in Figs. 11 and 12, we provide more result in abdominal multi-organ segmentation compared with other methods [3], [5], [22], [40].

B. Style-Transfer Network Architecture

The architecture of style-transfer network is shown in Fig. 8. Details for each module are shown in Tables IV, V, VI and VII. The abbreviations in the tables represent the following: h and w : height and width of the input images, n_s : dimension of the AdaIN parameters, N : the number of output channels, K : kernel size, S : stride size, P : padding size, FC: fully connected layer, IN: instance normalization, AdaIN: adaptive instance normalization, ReLU: rectified linear unit, LReLU: Leaky ReLU with a negative slope of 0.2.

C. Adaptive Instance Normalization (AdaIN)

Instance Normalization is defined as the following:

$$IN(x) = \gamma \left(\frac{x - \mu(x)}{\sigma(x)} \right) + \beta \quad (1)$$

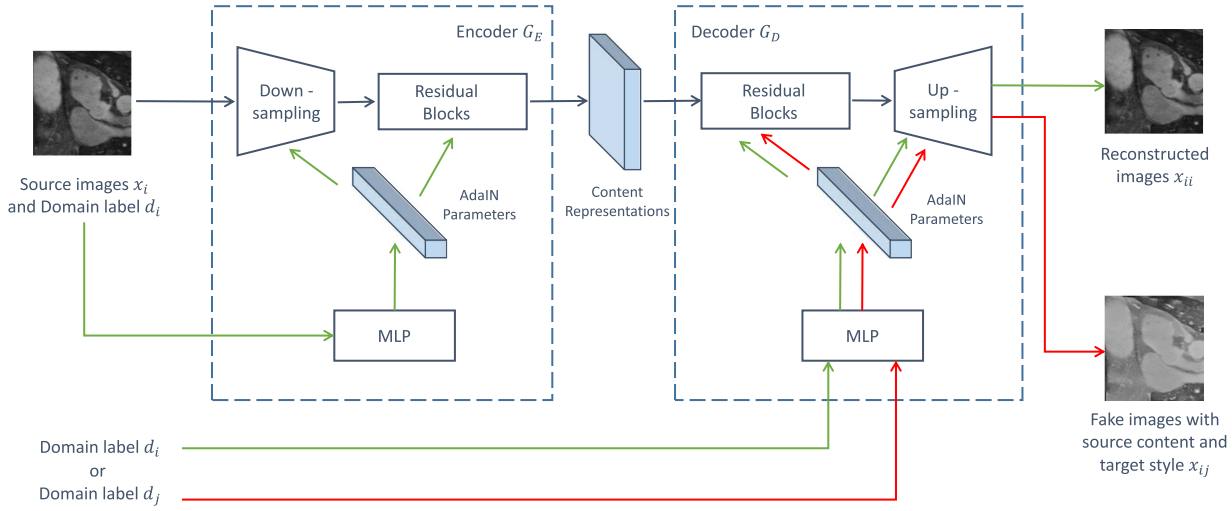


Fig. 8. Architecture of the style-transfer network.

TABLE IV
ARCHITECTURE OF THE UNIFIED CONTENT ENCODER \mathcal{G}_E

Part	Input → Output Shape	Layer Information
	(h,w,1)+(64+64) → (h,w,64)	CONV-(N64, K7x7, S1, P3), AdaIN, ReLU
Down-sampling	(h,w,64)+(128+128) → ($\frac{h}{2}, \frac{w}{2}, 128$)	CONV-(N128, K3x3, S2, P1), AdaIN, ReLU
	($\frac{h}{2}, \frac{w}{2}, 128$)+(256+256) → ($\frac{h}{4}, \frac{w}{4}, 256$)	CONV-(N256, K3x3, S2, P1), AdaIN, ReLU
Bottleneck	($\frac{h}{4}, \frac{w}{4}, 256$)+(256+256) → ($\frac{h}{4}, \frac{w}{4}, 256$)	ResBlock: CONV-(N256, K3x3, S1, P1), AdaIN, ReLU
	($\frac{h}{4}, \frac{w}{4}, 256$)+(256+256) → ($\frac{h}{4}, \frac{w}{4}, 256$)	ResBlock: CONV-(N256, K3x3, S1, P1), AdaIN, ReLU
	($\frac{h}{4}, \frac{w}{4}, 256$)+(256+256) → ($\frac{h}{4}, \frac{w}{4}, 256$)	ResBlock: CONV-(N256, K3x3, S1, P1), AdaIN, ReLU
	($\frac{h}{4}, \frac{w}{4}, 256$)+(256+256) → ($\frac{h}{4}, \frac{w}{4}, 256$)	ResBlock: CONV-(N256, K3x3, S1, P1), AdaIN, ReLU

TABLE V
ARCHITECTURE OF MLP FOR ENCODER \mathcal{G}_E AND DECODER \mathcal{G}_D

Part	Input → Output Shape	Layer Information
MLP	(2) → (256)	FC(2, 256), ReLU
	(256) → (256)	FC(256, 256), ReLU
	(256) → (n_s)	FC(256, n_s)

TABLE VI
ARCHITECTURE OF THE UNIFIED DECODER \mathcal{G}_D

Part	Input → Output Shape	Layer Information
Bottleneck	($\frac{h}{4}, \frac{w}{4}, 256$)+(256+256) → ($\frac{h}{4}, \frac{w}{4}, 256$)	ResBlock: CONV-(N256, K3x3, S1, P1), AdaIN, ReLU
	($\frac{h}{4}, \frac{w}{4}, 256$)+(256+256) → ($\frac{h}{4}, \frac{w}{4}, 256$)	ResBlock: CONV-(N256, K3x3, S1, P1), AdaIN, ReLU
	($\frac{h}{4}, \frac{w}{4}, 256$)+(256+256) → ($\frac{h}{4}, \frac{w}{4}, 256$)	ResBlock: CONV-(N256, K3x3, S1, P1), AdaIN, ReLU
	($\frac{h}{4}, \frac{w}{4}, 256$)+(256+256) → ($\frac{h}{4}, \frac{w}{4}, 256$)	ResBlock: CONV-(N256, K3x3, S1, P1), AdaIN, ReLU
Up-sampling	($\frac{h}{4}, \frac{w}{4}, 256$)+(128+128) → ($\frac{h}{2}, \frac{w}{2}, 128$)	DECONV-(N128, K3x3, S2, P1), AdaIN, ReLU
	($\frac{h}{2}, \frac{w}{2}, 128$)+(64+64) → (h,w,64)	DECONV-(N64, K3x3, S2, P1), AdaIN, ReLU
	(h,w,64)→(h,w,1)	CONV-(N1, K7x7, S1, P3), ReLU, Tanh

TABLE VII
ARCHITECTURE OF DOMAIN DISCRIMINATOR \mathcal{D}

Part	Input → Output Shape	Layer Information
Shared body	$(h, w, 1) \rightarrow (\frac{h}{2}, \frac{w}{2}, 64)$	CONV-(N64, K4x4, S2, P1), LReLU
	$(\frac{h}{2}, \frac{w}{2}, 64) \rightarrow (\frac{h}{4}, \frac{w}{4}, 128)$	CONV-(N128, K4x4, S2, P1), IN, LReLU
	$(\frac{h}{4}, \frac{w}{4}, 128) \rightarrow (\frac{h}{8}, \frac{w}{8}, 256)$	CONV-(N256, K4x4, S2, P1), IN, LReLU
	$(\frac{h}{8}, \frac{w}{8}, 256) \rightarrow (\frac{h}{8}, \frac{w}{8}, 512)$	CONV-(N512, K4x4, S1, P1), IN, LReLU
Output Branch D_1	$(\frac{h}{8}, \frac{w}{8}, 512) \rightarrow (\frac{h}{8}, \frac{w}{8}, 1)$	CONV-(N1, K4x4, S1, P1)
Output Branch D_2	$(\frac{h}{8}, \frac{w}{8}, 512) \rightarrow (\frac{h}{8}, \frac{w}{8}, 1)$	CONV-(N1, K4x4, S1, P1)

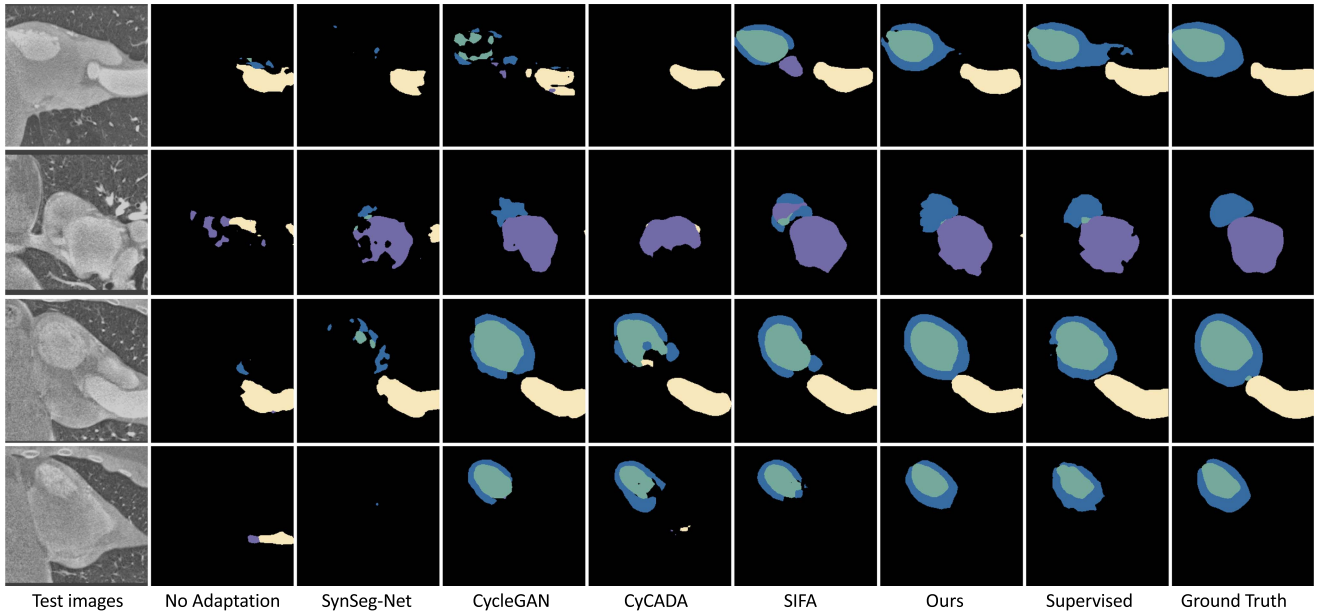


Fig. 9. Qualitative comparison result of cardiac MRI → CT segmentation.

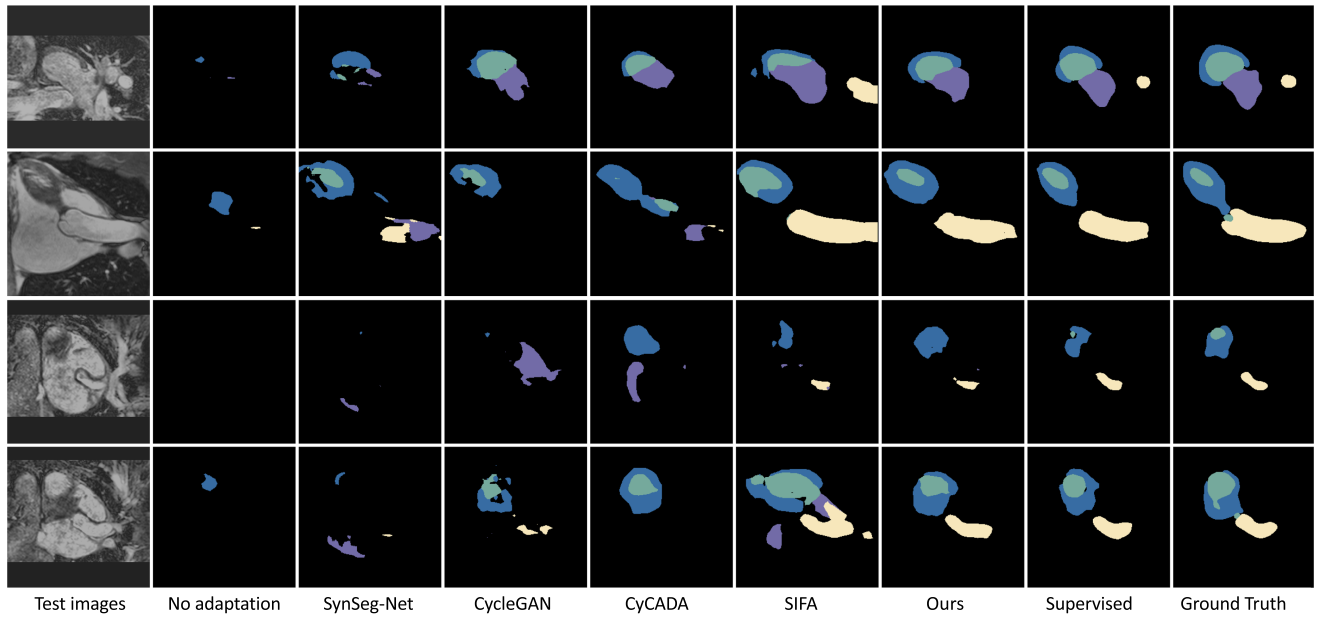


Fig. 10. Qualitative comparison result of cardiac CT → MRI segmentation.

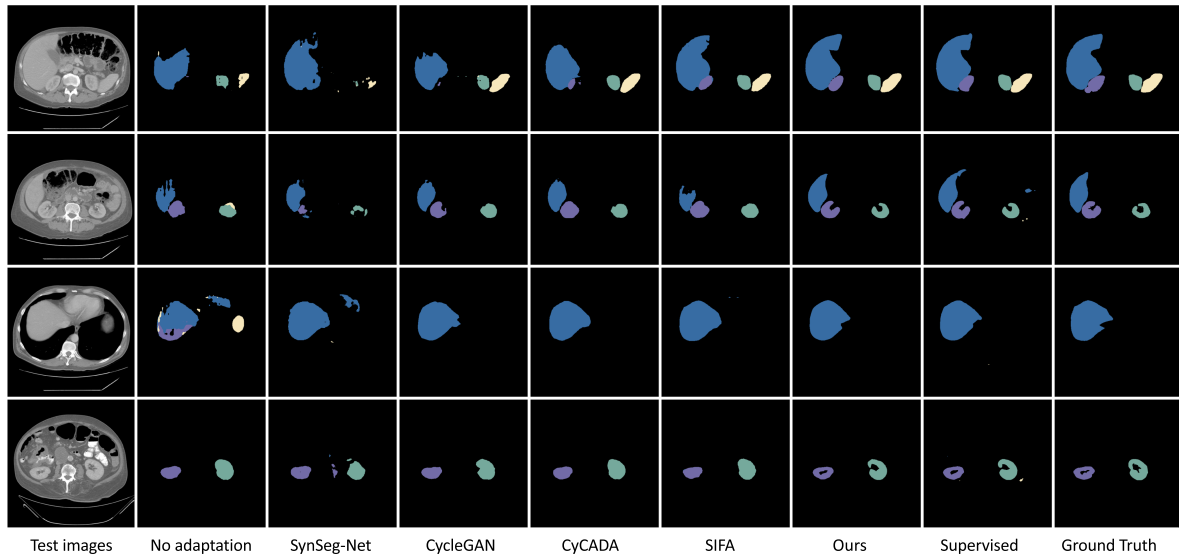


Fig. 11. Qualitative comparison result of abdominal MRI→CT segmentation.

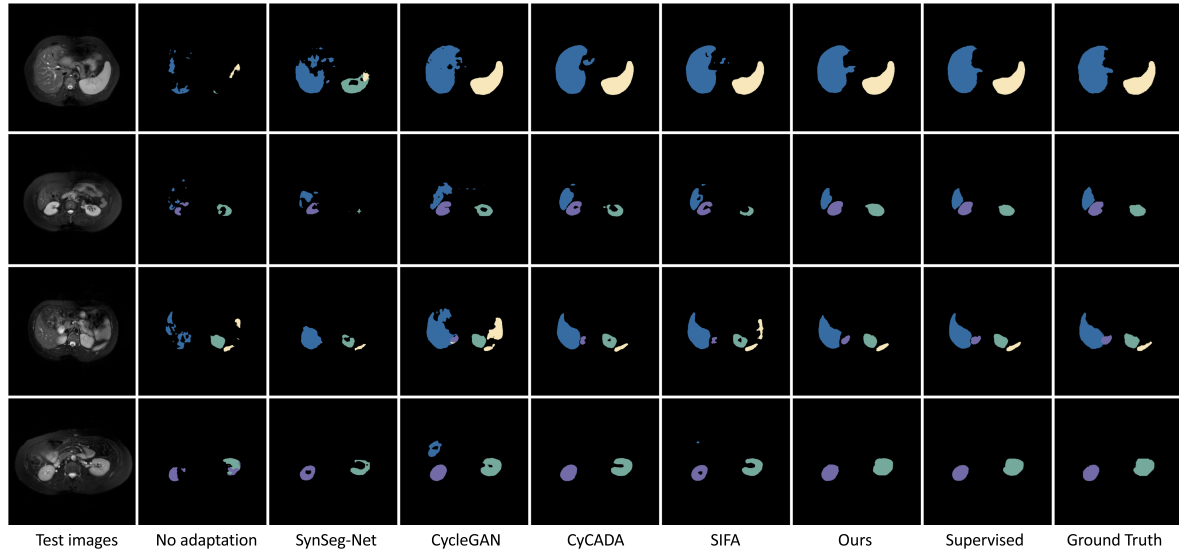


Fig. 12. Qualitative comparison result of abdominal CT→MRI segmentation.

where γ and β are learnable parameters, and $\mu(x)$ and $\sigma(x)$ are the channel-wise mean and variance which defined as:

$$\begin{aligned} \mu_{nc}(x) &= \frac{1}{HW} \sum_{h=1}^H \sum_{w=1}^W x_{nchw}, \sigma_{nc}(x) \\ &= \sqrt{\frac{1}{HW} \sum_{h=1}^H \sum_{w=1}^W (x_{nchw} - \mu_{nc}(x))^2}. \end{aligned} \quad (2)$$

According to previous works [36], [37], AdaIN receives a content input x and a style representation y , which contains y_μ and y_σ . Unlike Instance Normalization (IN), AdaIN has no learnable affine parameters. Instead, it uses the input style

representations as affine parameters adaptively:

$$AdaIN(x, y_\mu, y_\sigma) = y_\mu \left(\frac{x - \mu(x)}{\sigma(x)} \right) + y_\sigma. \quad (3)$$

REFERENCES

- [1] Y. Bengio, “Deep learning of representations for unsupervised and transfer learning,” in *Proc. ICML Workshop Unsupervised Transfer Learning. JMLR Workshop Conf. Proc.*, 2012, pp. 17–36.
- [2] Y. Ganin and V. Lempitsky, “Unsupervised domain adaptation by backpropagation,” in *Proc. IEEE/CVF Int. Conf. Mach. Learn.*, 2015, pp. 1180–1189.
- [3] J.-Y. Zhu, T. Park, P. Isola, and A. A. Efros, “Unpaired image-to-image translation using cycle-consistent adversarial networks,” in *Proc. IEEE/CVF Int. Conf. Comput. Vis.*, 2017, pp. 2223–2232.
- [4] M. Ghifary, W. B. Kleijn, M. Zhang, D. Balduzzi, and W. Li, “Deep reconstruction-classification networks for unsupervised domain adaptation,” in *Proc. Eur. Conf. Comput. Vis.*, 2016, pp. 597–613.

- [5] Y. Huo et al., "SynSeg-Net: Synthetic segmentation without target modality ground truth," *IEEE Trans. Med. Imag.*, vol. 38, no. 4, pp. 1016–1025, Apr. 2019.
- [6] Y.-H. Tsai, W.-C. Hung, S. Schulter, K. Sohn, M.-H. Yang, and M. Chandraker, "Learning to adapt structured output space for semantic segmentation," in *Proc. IEEE/CVF Conf. Comput. Vis. Pattern Recognit.*, 2018, pp. 7472–7481.
- [7] Y. Guo, X. Gu, and G.-Z. Yang, "MCDCD: Multi-source unsupervised domain adaptation for abnormal human gait detection," *IEEE J. Biomed. Health Inform.*, vol. 25, no. 10, pp. 4017–4028, Oct. 2021.
- [8] X. Zhuang and J. Shen, "Multi-scale patch and multi-modality atlases for whole heart segmentation of MRI," *Med. Image Anal.*, vol. 31, pp. 77–87, 2016.
- [9] C. Chen, Z. Zheng, X. Ding, Y. Huang, and Q. Dou, "Harmonizing transferability and discriminability for adapting object detectors," in *Proc. IEEE/CVF Conf. Comput. Vis. Pattern Recognit.*, 2020, pp. 8869–8878.
- [10] K. Saito, Y. Ushiku, T. Harada, and K. Saenko, "Strong-weak distribution alignment for adaptive object detection," in *Proc. IEEE/CVF Conf. Comput. Vis. Pattern Recognit.*, 2019, pp. 6956–6965.
- [11] M. Cordts et al., "The cityscapes dataset for semantic urban scene understanding," in *Proc. IEEE/CVF Conf. Comput. Vis. Pattern Recognit.*, 2016, pp. 3213–3223.
- [12] S. R. Richter, Z. Hayder, and V. Koltun, "Playing for benchmarks," in *Proc. IEEE Int. Conf. Comput. Vis.*, 2017, pp. 2232–2241, doi: [10.1109/ICCV.2017.243](https://doi.org/10.1109/ICCV.2017.243).
- [13] A. Emre Kavur et al., "Chaos challenge—combined (CT-MR) healthy abdominal organ segmentation," *Med. Image Anal.*, vol. 69, 2020, Art. no. 101950.
- [14] B. Landman, Z. Xu, J. E. Iglesias, M. Styner, T. R. Langerak, and A. Klein, "Multi-atlas labeling beyond the cranial vault-workshop and challenge," 2017, [Online]. Available: <https://www.synapse.org/Synapse:syn3193805/wiki/217789>
- [15] J. M. J. Valanarasu, P. Oza, I. Hacihaliloglu, and V. M. Patel, "Medical transformer: Gated axial-attention for medical image segmentation," in *Med. Image Comput. Comput. Assist. Interv., Proc. 24th Int. Conf.*, Strasbourg, France, Sep./Oct. 2021, pp. 36–46.
- [16] Z. Zhou, M. M. R. Siddiquee, N. Tajbakhsh, and J. Liang, "Unet : A nested U-net architecture for medical image segmentation," in *Proc. Deep Learn. Med. Image Anal. Multimodal Learn. Clin. Decis. Support*, 2018, pp. 3–11.
- [17] Z. Gu et al., "CE-Net: Context encoder network for 2D medical image segmentation," *IEEE Trans. Med. Imag.*, vol. 38, no. 10, pp. 2281–2292, Oct. 2019.
- [18] C. Chen, Q. Dou, H. Chen, J. Qin, and P. A. Heng, "Unsupervised bidirectional cross-modality adaptation via deeply synergistic image and feature alignment for medical image segmentation," *IEEE Trans. Med. Imag.*, vol. 39, no. 7, pp. 2494–2505, Jul. 2020.
- [19] T. Wollmann, C. S. Eijkman, and K. Rohr, "Adversarial domain adaptation to improve automatic breast cancer grading in lymph nodes," in *Proc. IEEE 15th Int. Symp. Biomed. Imag.*, 2018, pp. 582–585.
- [20] I. Manakov, M. Rohm, C. Kern, B. Schworm, K. Kortuem, and V. Tresp, "Noise as domain shift: Denoising medical images by unpaired image translation," in *Proc. Domain Adapt. Representation Transfer Med. Image Learn. Less Labels Imperfect Data*, 2019, pp. 3–10.
- [21] F. Mahmood, R. Chen, and N. J. Durr, "Unsupervised reverse domain adaptation for synthetic medical images via adversarial training," *IEEE Trans. Med. Imag.*, vol. 37, no. 12, pp. 2572–2581, Dec. 2018.
- [22] C. Chen, Q. Dou, H. Chen, J. Qin, and P.-A. Heng, "Synergistic image and feature adaptation: Towards cross-modality domain adaptation for medical image segmentation," in *Proc. AAAI Conf. Artif. Intell.*, vol. 33, no. 01, 2019, pp. 865–872.
- [23] Z. Liu, Z. Zhu, S. Zheng, Y. Liu, J. Zhou, and Y. Zhao, "Margin preserving self-paced contrastive learning towards domain adaptation for medical image segmentation," *IEEE J. Biomed. Health Inform.*, vol. 26, no. 2, pp. 638–647, Feb. 2022.
- [24] X. Han et al., "Deep symmetric adaptation network for cross-modality medical image segmentation," *IEEE Trans. Med. Imag.*, vol. 41, no. 1, pp. 121–132, Jan. 2022.
- [25] W. Hong, Z. Wang, M. Yang, and J. Yuan, "Conditional generative adversarial network for structured domain adaptation," in *Proc. IEEE/CVF Conf. Comput. Vis. Pattern Recognit.*, 2018, pp. 1335–1344.
- [26] B. Benjdira, Y. Bazi, A. Koubaa, and K. Ouni, "Unsupervised domain adaptation using generative adversarial networks for semantic segmentation of aerial images," *Remote Sens.*, vol. 11, no. 11, 2019, Art. no. 1369.
- [27] Y. Zhang, T. Liu, M. Long, and M. Jordan, "Bridging theory and algorithm for domain adaptation," in *Proc. Int. Conf. Mach. Learn.*, 2019, pp. 7404–7413.
- [28] M. Li, Y.-M. Zhai, Y.-W. Luo, P.-F. Ge, and C.-X. Ren, "Enhanced transport distance for unsupervised domain adaptation," in *Proc. IEEE/CVF Conf. Comput. Vis. Pattern Recognit.*, 2020, pp. 13936–13944.
- [29] Y. Zou, Z. Yu, B. Kumar, and J. Wang, "Unsupervised domain adaptation for semantic segmentation via class-balanced self-training," in *Proc. Eur. Conf. Comput. Vis.*, 2018, pp. 289–305.
- [30] Q. Lian, F. Lv, L. Duan, and B. Gong, "Constructing self-motivated pyramid curriculums for cross-domain semantic segmentation: A non-adversarial approach," in *Proc. IEEE/CVF Int. Conf. Comput. Vis.*, 2019, pp. 6758–6767.
- [31] Y. Luo, L. Zheng, T. Guan, J. Yu, and Y. Yang, "Taking a closer look at domain shift: Category-level adversaries for semantics consistent domain adaptation," in *Proc. IEEE/CVF Conf. Comput. Vis. Pattern Recognit.*, 2019, pp. 2507–2516.
- [32] F. Yu, M. Zhang, H. Dong, S. Hu, B. Dong, and L. Zhang, "Dast: Unsupervised domain adaptation in semantic segmentation based on discriminator attention and self-training," in *Proc. AAAI Conf. Artif. Intell.*, vol. 35, no. 12, 2021, pp. 10754–10762.
- [33] J. Huang, S. Lu, D. Guan, and X. Zhang, "Contextual-relation consistent domain adaptation for semantic segmentation," in *Proc. 16th Eur. Conf. Comput. Vis.*, 2020, pp. 705–722.
- [34] W. Qiang, J. Li, C. Zheng, B. Su, and H. Xiong, "Robust local preserving and global aligning network for adversarial domain adaptation," *IEEE Trans. Knowl. Data Eng.*, vol. 35, no. 3, pp. 3014–3029, Mar. 2023.
- [35] Y. Choi, M. Choi, M. Kim, J.-W. Ha, S. Kim, and J. Choo, "Stargan: Unified generative adversarial networks for multi-domain image-to-image translation," in *Proc. IEEE/CVF Conf. Comput. Vis. Pattern Recognit.*, 2018, pp. 8789–8797.
- [36] X. Huang, M.-Y. Liu, S. Belongie, and J. Kautz, "Multimodal unsupervised image-to-image translation," in *Proc. Eur. Conf. Comput. Vis.*, 2018, pp. 172–189.
- [37] X. Huang and S. Belongie, "Arbitrary style transfer in real-time with adaptive instance normalization," in *Proc. IEEE/CVF Int. Conf. Comput. Vis.*, 2017, pp. 1501–1510.
- [38] P. Isola, J.-Y. Zhu, T. Zhou, and A. A. Efros, "Image-to-image translation with conditional adversarial networks," in *Proc. IEEE/CVF Conf. Comput. Vis. Pattern Recognit.*, 2017, pp. 1125–1134.
- [39] L.-C. Chen, G. Papandreou, I. Kokkinos, K. Murphy, and A. L. Yuille, "Deeplab: Semantic image segmentation with deep convolutional nets, atrous convolution, and fully connected CRFs," *IEEE Trans. Pattern Anal. Mach. Intell.*, vol. 40, no. 4, pp. 834–848, Apr. 2018.
- [40] J. Hoffman et al., "Cycada: Cycle-consistent adversarial domain adaptation," in *Proc. Int. Conf. Mach. Learn.*, 2018, pp. 1989–1998.
- [41] D. Zou, Q. Zhu, and P. Yan, "Unsupervised domain adaptation with dual-scheme fusion network for medical image segmentation," in *Proc. Int. Joint Conf. Artif. Intell.*, 2020, pp. 3291–3298.
- [42] J. Liu et al., "Automated cardiac segmentation of cross-modal medical images using unsupervised multi-domain adaptation and spatial neural attention structure," *Med. Image Anal.*, vol. 72, 2021, Art. no. 102135.
- [43] X. Chen et al., "Diverse data augmentation for learning image segmentation with cross-modality annotations," *Med. Image Anal.*, vol. 71, 2021, Art. no. 102060.
- [44] C. Bian et al., "Uncertainty-aware domain alignment for anatomical structure segmentation," *Med. Image Anal.*, vol. 64, 2020, Art. no. 101732.
- [45] X. Du and Y. Liu, "Constraint-based unsupervised domain adaptation network for multi-modality cardiac image segmentation," *IEEE J. Biomed. Health Inform.*, vol. 26, no. 1, pp. 67–78, Jan. 2022.
- [46] D. P. Kingma and J. Ba, "Adam: A method for stochastic optimization," 2014, *arXiv:1412.6980*.
- [47] H.-Y. Lee et al., "Drit : Diverse image-to-image translation via disentangled representations," *Int. J. Comput. Vis.*, vol. 128, no. 10, pp. 2402–2417, 2020.
- [48] Y. Choi, Y. Uh, J. Yoo, and J.-W. Ha, "Stargan v2: Diverse image synthesis for multiple domains," in *Proc. IEEE/CVF Conf. Comput. Vis. Pattern Recognit.*, 2020, pp. 8188–8197.